EDGE ARTICLE

Check for updates

Enhancing local K⁺ adsorption by high-density cube corners for efficient electroreduction of CO₂ to C₂₊ products†

Hu Zang,[a] Changjiang Liu,[a] Qinyuan Ji,[a] Jiahao Wang,[a] Haiyan Lu,[a] Nan Yu[a] and Baoyou Geng [ID] *[ab]

Reducing carbon dioxide (CO_2) to high value-added chemicals using renewable electricity is a promising approach to reducing CO_2 levels in the air and mitigating the greenhouse effect, which depends on high-efficiency electrocatalysts. Copper-based catalysts can be used for electroreduction of CO_2 to produce C_{2+} products with high added value, but suffer from poor stability and low selectivity. Herein, we propose a strategy to enhance the field effect by varying the cubic corner density on the surface of Cu_2O microspheres for improving the electrocatalytic performance of CO_2 reduction to C_{2+} products. Finite element method (FEM) simulation results show that the high density of cubic corners helps to enhance the local electric field, which increases the K^+ concentration on the catalyst surface. The results of CO_2 electroreduction tests show that the $FE_{C_{2+}}$ of the Cu_2O catalyst with high-density cubic corners is 71% at a partial current density of 497 mA cm^{-2}. Density functional theory (DFT) calculations reveal that Cu_2O (111) and Cu_2O (110) can effectively reduce the energy barrier of C–C coupling and improve the $FE_{C_{2+}}$ at high K^+ concentrations relative to Cu_2O (100). This study provides a new perspective for the design and development of efficient CO_2RR catalysts.

Introduction

The massive extraction and utilization of fossil fuels has brought about a dramatic increase in the amount of CO_2 in the atmosphere, leading to global warming and climate change, which poses serious environmental problems.[1] The efficient capture and recycling of CO_2 is widely recognized as the key to mitigating environmental problems related to the greenhouse effect and sea level rise, and promoting sustainable development.[2–4] In recent years, it has been found that the electrochemical conversion of CO_2 into C_{2+} products with high application value, using renewable electricity, is one of the most promising technologies for realizing the carbon cycle.[5–12] Currently, Cu-based catalysts are attracting attention as the only catalysts that can realize C–C coupling and electroreduction of CO_2 to C_{2+} products.[13–21]

Nevertheless, the thermodynamics and kinetics of C–C coupling are relatively slow in the CO_2RR.[8,22–26] Therefore, modification of Cu-based catalysts, such as crystal surface modulation,[27–29] surface restructuring,[30–33] and oxidation state optimization,[16,34–36] to improve the efficiency of C_{2+} products remains a hot topic and challenge. The adjustment of the crystal surface or surface structure has a significant effect on improving the performance of Cu-based catalysts.[37] On the one hand, the exposed faces of Cu-based catalysts have a great influence on the catalytic activity and selectivity in the CO_2RR process.[38,39] On the other hand, the field effect induced by the tip structure of Cu-based catalysts plays an important role in the CO_2RR process.[40–42] Numerous studies have found that the active sites of the CO_2RR are usually located on the top corners and ridges of the catalysts.[43–45] Previous reports have focused on the effects of vertex curvature or array orientation on the field effect; however, the vertices and ridges on the exposed surface are particularly critical to catalytic activity and selectivity, while the effects of vertex density or tip-exposed crystal faces on the catalyst surface for the catalytic performance have been rarely reported, and also their effects on the CO_2RR are unknown.

Herein, we investigated the effect of the density of cubic corners on the field effect with FEM simulations, and the effect of the vertices and ridges on the cubic corners on the catalytic performance was studied by DFT calculations. The FEM simulation results found that the higher density of the cube corners had a stronger influence on the field effect, which is favorable

[a] College of Chemistry and Materials Science, The Key Laboratory of Functional Molecular Solids, Ministry of Education, The Key Laboratory of Electrochemical Clean Energy of Anhui Higher Education Institutes, Anhui Provincial Engineering Laboratory for New-Energy Vehicle Battery Energy-Storage Materials, Anhui Normal University, Jiuhua Road 189, Wuhu, 241002, China. E-mail: bygeng@mail.ahnu.edu.cn

[b] Institute of Energy, Hefei Comprehensive National Science Center, Hefei, 230031, China

for the aggregation and adsorption of K^+. In the experiment, we prepare a Cu_2O microsphere with cubic corners on the surface,[46] which is the same as the results of FEM simulation. DFT calculations demonstrate that, at stronger electric fields and higher K^+ concentrations, the Cu_2O (111) and (110) faces on the cube corner contribute to the adsorption and C–C coupling of *CO intermediates, as well as to the desorption of C_{2+} products. This work fills the gap in the application of the localized electric field induced by different density nano-arrays in CO_2 electroreduction, and also illustrates the roles of vertices and ridges on the exposed crystal in CO_2 electroreduction, which provides new perspectives for the design of efficient CO_2RR catalysts and contributes to the mitigation of environmental problems caused by greenhouse gases.

Results and discussion

FEM simulation

We used COMSOL Multiphysics field simulations to investigate the effect of the density of cubic corners on the local electric field and K^+ concentration. Five models with different cube corner densities (Fig. S1†) were developed using FEM, and the localized electric field and K^+ concentration on their cube corners were also investigated.

As shown in Fig. 1a–c and S2–S4,† significant local electric field aggregation effects can be observed for a single cube corner. According to the principle of electric field superposition, as the number of cube corners increases, the electric field strength of the cube angle shows an increasing trend. M3 is a microsphere composed of cubic inflections (Fig. 1c), which has the highest density of cubic corners and the maximum localized electric field strength of 565 V m^{-1}. We simulated the K^+ concentration on the cubic corner surface using the transport of diluted species (tds) physics modules in COMSOL Multiphysics. From Fig. 1a and

b and S5–S7,† it is found that the distribution of K^+ concentration is positively correlated with the distribution of local electric field strength. As the local electric field intensity increases, the K^+ concentration on the cube corner surface gradually increases, with M3 having the maximum K^+ concentration of 3.39 M. The localized electric field facilitates the adsorption and aggregation of K^+, which is mainly caused by the field effect induced reagent concentration, because positively charged K^+ will be aggregated on the corner surfaces of the cube possessing a strong negative electric field under electrostatic action. The high concentrations of K^+ facilitate the adsorption of CO_2 and the generation of C_{2+} products (Fig. 1d).

Catalyst synthesis and characterization

Cu_2O-X microspheres with cube corners were synthesized using a solvothermal method (X is the volume of water used, which is 0, 0.5, 1, 2, 4, and 10 mL respectively, and the corresponding samples are named Cu_2O-0, Cu_2O-0.5, Cu_2O-1, Cu_2O-2, Cu_2O-4, and Cu_2O-10, respectively). The synthesis mechanism and synthesis process of Cu_2O-0 are shown in Fig. 2a and S8.† In order to better observe the growth mechanism of the Cu_2O-0 catalyst, its liquid color and product morphology were investigated over time during the synthesis process (Fig. S9†). The scanning electron microscopy (SEM) images of Cu_2O-0 are shown in Fig. 2b and c, and it can be seen that the surface of Cu_2O-0 microspheres has a large number of cube corners. The transmission electron microscopy (TEM) image (Fig. 2d) shows more visually that Cu_2O-0 consists of microspheres with numerous vertices and ridges on the surface. The angles of the vertices are mostly 90°, which better indicates that the tips of the surface on the Cu_2O-0 microspheres are cubic inflection corners. From the inset in Fig. 2b, the air/water contact angle of Cu_2O-0 is 141°, which indicates that it has good hydrophobicity. Fig. S10† shows the air/water contact angle of Cu_2O-X. Fig. 2e–g show the high-resolution TEM (HRTEM) images of Cu_2O-0. Fig. 2e shows the Cu_2O crystal planes at the corners of different cubes (as shown in the inset). HRTEM images (Fig. 2f and g) and FFT patterns (inset) show that the lattice spaces are 0.301, 0.246 and 0.213 nm respectively, which can be well matched with the (110), (111) and (200) crystal planes of cubic Cu_2O. The SEM and HRTEM analyses showed that the morphology of Cu_2O-X did not change significantly with increasing water content (Fig. S11†). The peaks located at 29.6°, 36.4°, and 42.3° correspond to the (110), (111), and (200) crystal planes of Cu_2O (JCPDS: PDF#99-0041), respectively, which indicates that the synthesized material is predominantly Cu_2O and has a good crystallinity (Fig. 2h). Fig. S12† shows that the Cu_2O-X catalysts with different water contents have the same Cu_2O phase. Fig. 2i shows that Cu is predominantly +1-valent, some of which is +2-valent; the Cu^{2+} in the XPS is most likely caused by the oxidation of the Cu_2O when it is exposed in the air. In summary, the synthesized catalysts are consistent with the FEM model.
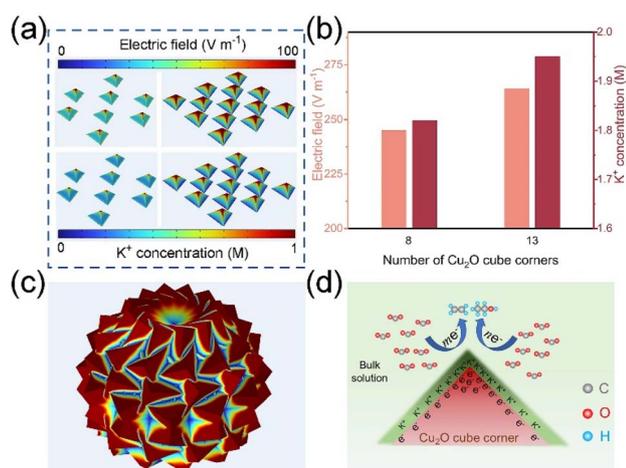
Electrochemical CO_2RR performance evaluation

Tests of the CO_2 electroreduction properties of the catalysts were performed in a flow cell (Fig. S13†). The linear sweep
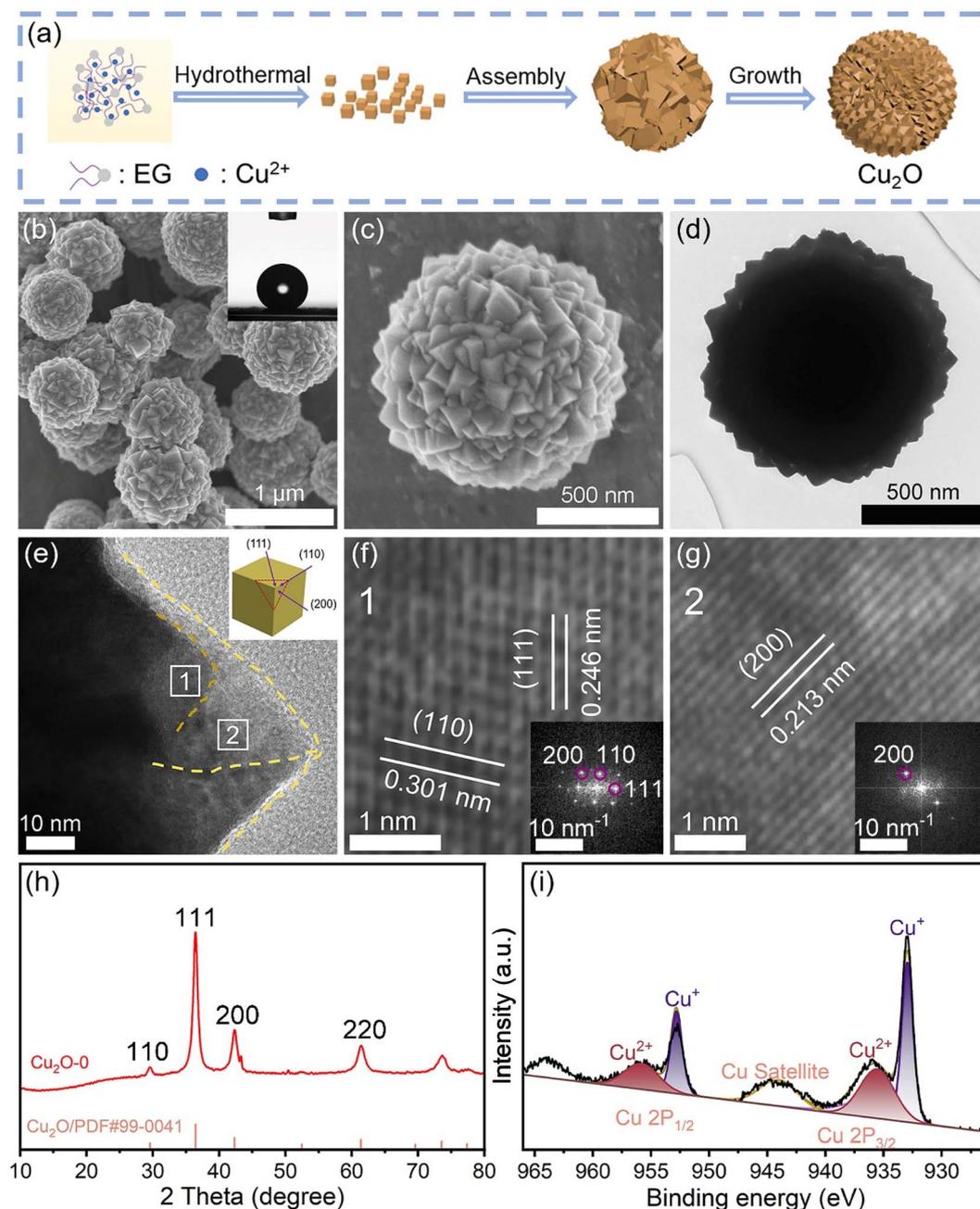

Fig. 1 (a) The electric field (upper half) and K^+ concentration (lower half) distribution on M-4 and M-5 through COMSOL Multiphysics simulations. (b) The electric field and K^+ concentration at the tips of M-4 and M-5. (c) The electric field distribution on M-3. (d) A schematic illustration of the local electric field and K^+ ions on the Cu_2O cube corner for promoting C_2 formation.

Fig. 2 (a) Schematic formation mechanism of the Cu_2O-0 catalyst. (b and c) SEM images of the Cu_2O-0 catalyst. (d) TEM image of the Cu_2O-0 catalyst. (e–g) HRTEM images of the Cu_2O-0 catalyst. (h) The XRD pattern of the Cu_2O-0 catalyst. (i) The XPS spectrum of the Cu_2O-0 catalyst.

voltammetry (LSV) test results (Fig. 3a and S14†) show that Cu_2O-0 has greater positive onset potential and greater negative current density, indicating that Cu_2O-0 has higher CO_2RR activity. The liquid and gas products were examined by ^1H NMR spectroscopy (Fig. S15†) and gas chromatography (GC) (Fig. S16 and S17†), respectively. In terms of product distribution, the reduction products of all Cu_2O-X catalysts had the same trend with increasing applied current, with the faradaic efficiency (FE) of C_{2+} increasing and then decreasing, and the FE of H_2 decreasing and then increasing (Fig. 3b and S18†). From Fig. 3c and d, it was found that the Cu_2O-0 catalyst possessed the

largest $FE_{C_{2+}}$ and the smallest FE_{H_2}. The $FE_{C_{2+}}$ and FE_{H_2} of the Cu_2O-0 catalyst were 71% and 12% at a partial current density of 497 mA cm^{-2}, respectively. Moreover, the $FE_{C_{2+}}$ of the Cu_2O-0 catalyst was 1.8 times higher than the $FE_{C_{2+}}$ of the Cu_2O-10 catalyst.

We have conducted multiple studies to better understand the differences in catalytic performance of different Cu_2O-X catalysts. By recording the cyclic voltammetry curves (Fig. S19†) of Cu_2O-X catalysts at different scan rates in the non-Faraday zone, their double-layer capacitance (C_{dl}) (Fig. S20†) was calculated, which was used to estimate their surface roughness
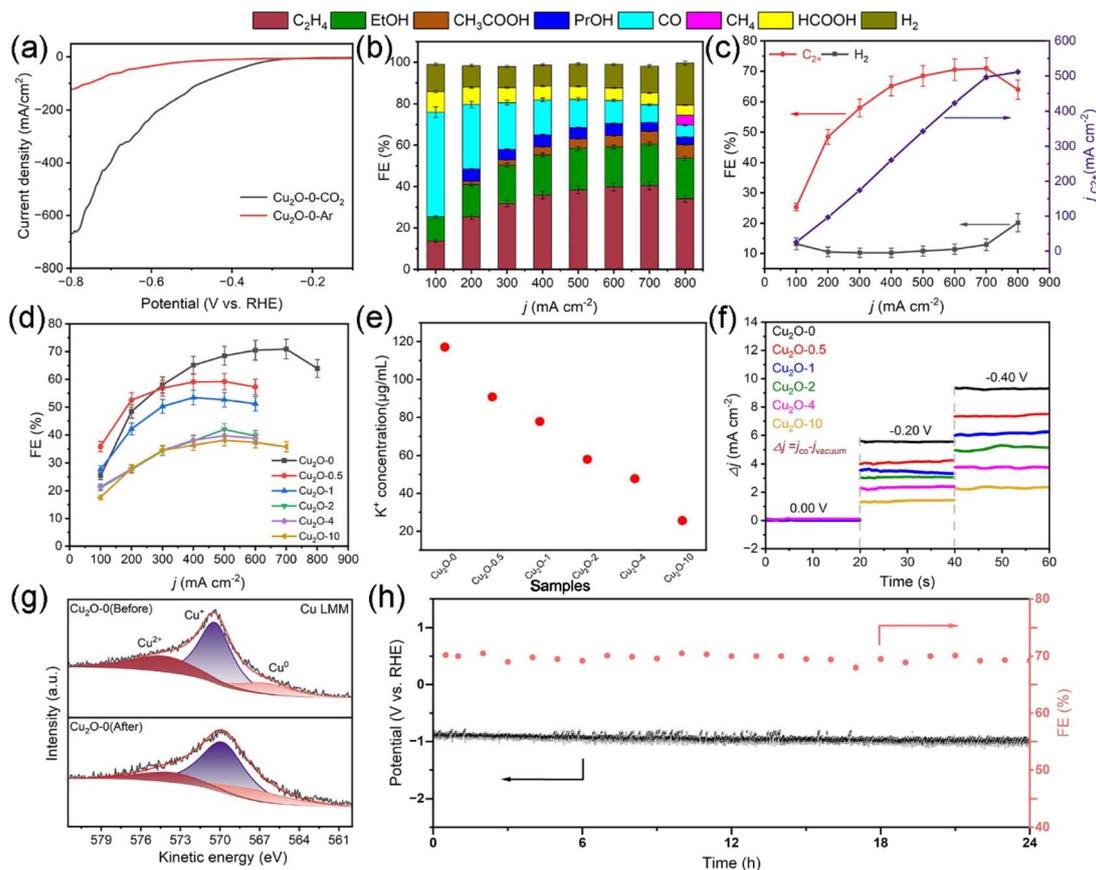
Fig. 3 (a) The LSV curves of the Cu_2O-0 catalyst under an N_2 atmosphere and CO_2 atmosphere. (b) FEs of various products on the Cu_2O-0 catalyst during the CO_2RR at different current densities. (c) C_{2+} and H_2 FEs and current densities *vs.* applied potential of the Cu_2O-0 catalyst. (d) C_{2+} FEs of Cu_2O-X catalysts. (e) Comparison of the adsorbed-K^+ concentration on Cu_2O-X catalysts. (f) Results of CO adsorption responses on Cu_2O-X catalysts under different applied voltages. (g) Deconvoluted Cu Auger LMM spectra of the Cu_2O-0 catalyst before and after the CO_2RR. (h) CO_2RR stability on the Cu_2O-0 catalyst at 700 mA cm^{-2}.

coefficient (R_f) and electrochemically active surface area (ECSA) (Fig. S21 and Table S1†). The results showed that the Cu_2O-0 catalyst had the largest C_{dl} (42.8 mF cm^{-2}), R_f (713.3), and ECSA (713.3 cm^2), thus indicating that the Cu_2O-0 catalyst can produce more active sites than other Cu_2O-X catalysts, which is more favorable for the CO_2RR. Meanwhile, Fig. S22† shows that the Cu_2O-0 catalyst has the smallest Tafel slope, which also indicates that the Cu_2O-0 catalyst has the best CO_2RR performance.

According to the FEM simulation results, it is illustrated that the high density of cubic corners contributes to the adsorption of K^+ and CO. To validate the FEM simulation results and to demonstrate the advantages of high-density cubic corners, we performed K^+ and CO adsorption experiments (schematic shown in Fig. S23 and S24†). Fig. 3e and f and Table S2† show that the adsorption capacity of K^+ and CO on the Cu_2O-X catalysts increases gradually with the increase of the cube corner density, and the Cu_2O-0 catalyst has the largest cube corner density and the strongest K^+ and CO adsorption capacity.

As shown in Fig. 3h, the Cu_2O-0 catalyst also exhibited excellent long-term stability, operating at a constant current density of 700 mA cm^{-2} for 24 h without a significant change in

the applied voltage or $FE_{C_{2+}}$, with the $FE_{C_{2+}}$ remaining around 70%. In order to better understand the long-term stability and selectivity of the Cu_2O-0 catalyst, SEM, XRD, and XPS were used to characterize the Cu_2O-X catalyst before and after the CO_2RR. From Fig. S25,† the morphology of the Cu_2O-0 catalyst was almost unchanged before and after the CO_2RR. XRD (Fig. S26 and S27†) patterns showed that the physical phase of the Cu_2O-0 catalyst was maintained before and after the reaction. The Cu Auger LMM spectra (Fig. 3g and S28†) were recorded and deconvoluted to distinguish Cu^+ and Cu^0 before and after the CO_2RR.[47] The ratio of the Cu^0 fraction increased from 17.14% to 20.23%, and the ratio of the Cu^+ fraction decreased from 68.72% to 65.34% in the Cu_2O-0 catalyst. The Cu Auger LMM spectra illustrated that Cu^+ in the Cu_2O-0 catalyst was well maintained during the CO_2RR process. The reason for Cu^+ being maintained in the Cu_2O-0 catalyst may be due to the high density of cubic corners on the Cu_2O-0 catalyst microspheres, which gives the surface a strong localized electric field and high K^+ concentration, leading to accelerated electron transport on the cubic corner surface and the inhibition of the redox reaction of Cu^+/Cu^0.[47] These lead to the excellent selectivity and long-term stability of the Cu_2O-0 catalyst.

In situ Raman and in situ FT-IR measurements

To further understand the reaction mechanism of the CO_2RR, we performed in situ Raman and in situ FT-IR tests on the Cu_2O-0 and Cu_2O-4 during the CO_2RR. The in situ Raman testing equipment is shown in Fig. S29.† As shown in Fig. 4a and S30a,† Cu_2O-0 and Cu_2O-4 show two peaks around ~280 and ~365 cm^{-1}, which are caused by the rotational and stretching vibrations of *CO on the Cu active site after applying the voltage.[48–50] In addition, the Cu_2O-0 and Cu_2O-4 catalysts have three peaks associated with $Cu^{\delta+}$ near ~415, ~520, and ~620 cm^{-1} in the low-energy region (Fig. 4b and S30b†), corresponding to the modes resulting from a multi-phonon process – the T_{2g} vibrational mode and the T_{1u} mode of Cu_2O.[47,49,51–55] With the increase of applied potential, the Cu^+ characteristic peaks (~520 cm^{-1}) of Cu_2O-0 catalysts are well preserved, and this is consistent with the XRD (Fig. S26†) and XPS (Fig. 3g) results measured before and after the CO_2RR, fully indicating that the Cu valence state in the Cu_2O-0 catalyst is stable during the CO_2RR process. In the high-energy region, the signals near ~1015 and ~1066 cm^{-1} are attributed to the adsorption of HCO_3^- and CO_3^{2-} (Fig. 4c and S30c†),[50,56] respectively, which are formed on the surface of the catalyst after CO_2 is dissolved in the electrolyte. The local hydrogen proton concentration and local microenvironment around the catalysts during the CO_2RR were evaluated by monitoring the ratio of HCO_3^- and CO_3^{2-} adsorbed on the catalyst surface (Fig. S31†).[56,57] The results show that the local hydrogen proton

depletion on the surface of the Cu_2O-0 catalyst is more stable than that of the Cu_2O-4 catalyst, thus maintaining the stability of the local microenvironment and the durability of the C_{2+} products on the catalyst.[50] In addition, the signals generated in the regions around ~1840 cm^{-1} and ~2060 cm^{-1} belong to the bridge-boundary *CO (*CO$_{bridge}$) and top-boundary *CO (*CO$_{atop}$) conformations,[48,58] respectively. As the cathode applied voltage became more negative, the *CO$_{bridge}$ signal on the Cu_2O-0 catalyst changed weakly (Fig. 4d), and the *CO$_{bridge}$ signal on the Cu_2O-4 catalyst basically disappeared (Fig. S30d†), suggesting that most of the *CO intermediates were bound at the top and a small portion of them were bound at the bridge sites in the Cu_2O-0 catalyst, whereas the *CO intermediates were mainly from the top of the Cu_2O-4 catalyst. The mixing of *CO$_{bridge}$ and *CO$_{atop}$ is more favorable for the C–C coupling.[59,60] Therefore, the *CO intermediates on the Cu_2O-0 catalyst are more favorable for C–C coupling and the production of C_{2+} products.

The *CO$_{atop}$ intermediates on the catalyst can be divided into low and high frequency bands (LFB and HFB). According to previous studies, the signal in the LFB belongs to a dynamic *CO intermediate, which contributes to subsequent C–C coupling. The HFB stretching band is attributed to the separated static *CO intermediate, which makes it difficult to perform C–C coupling.[48,60] As seen in Fig. 4e, we compared the LFB and HFB band intensities. The low/high value of the Cu_2O-0 catalyst is larger than that of the Cu_2O-4 catalyst, indicating
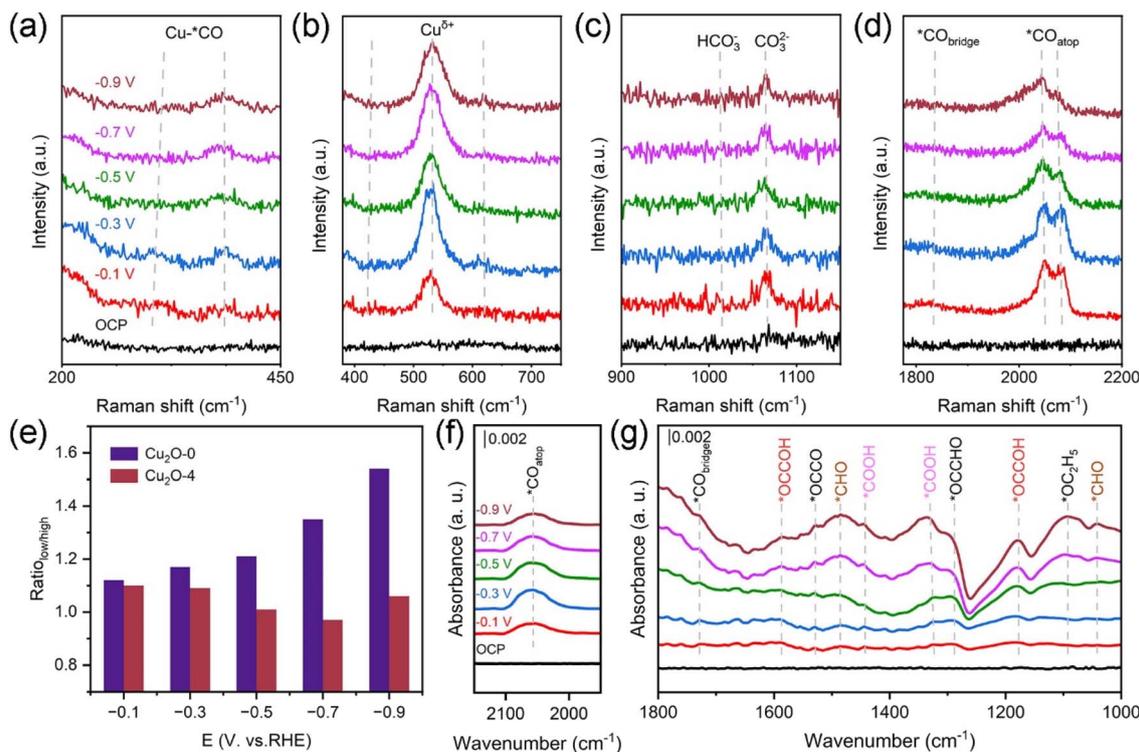

Fig. 4 In situ Raman spectra of the Cu_2O-0 catalyst in the range 200–450 cm^{-1} (a), 400–750 cm^{-1} (b), 900–1150 cm^{-1} (c) and 1800–2200 cm^{-1} (d) at various applied potentials (vs. RHE). (e) Ratio of the low-frequency and high-frequency bands in the range 2000–2200 cm^{-1} of Cu_2O-0 and Cu_2O-4 catalysts at various applied potentials. (f and g) In situ FT-IR spectra of the Cu_2O-0 catalyst at various applied potentials (vs. RHE).

that the Cu_2O-0 catalyst is more favorable for C–C coupling and C_{2+} product generation.[50] Through observing the changes in the intensity of the $*CO_{atop}$ peaks, it is found that as the external applied voltage becomes more negative, the $*CO$ intermediates first accumulate, then C–C coupling generates C_{2+} products on the Cu_2O-0 catalyst. Due to the involvement of more $*CO$ intermediates in C–C coupling, the $*CO$ peak intensity shows a decreasing trend on the Cu_2O-0 catalyst (Fig. 4d),[61] while the relative intensity of the HFB (Fig. S30d†) tends to increase at higher potentials on the Cu_2O-4 catalyst, indicating an increase in static $*CO$ intermediates and a decrease in C–C coupling ability on the Cu_2O-4 catalyst.[48] This is consistent with the electrochemical CO_2RR results.

In situ FT-IR tests was performed to investigate the reaction pathways of the C_{2+} products (Fig. S32†). In Fig. 4f and g and S33,† the peaks at $\sim$1720 and $\sim$2050 cm^{-1} are the characteristic peaks of $*CO_{bridge}$ and $*CO_{atop}$,[62,63] respectively. This is the same species of $*CO$ intermediates observed in *in situ* Raman spectra. The characteristic peaks at $\sim$1330 and $\sim$1440 cm^{-1} belong to the C–OH and C–O stretching modes of $*COOH$ intermediates, respectively, which help to generate $*CO$ intermediates on the catalysts.[64,65] Compared with Cu_2O-4, the $*COOH$ peak intensity on Cu_2O-0 is significantly stronger, but its $*CO_{atop}$ peak intensity is weak, indicating that the $*CO$ intermediates produced by $*COOH$ on Cu_2O-0 are more involved in C–C coupling and C_{2+} products.[66] The absorption peaks near $\sim$1090, $\sim$1180 and $\sim$1590 cm^{-1} are attributed to $*OC_2H_5$ and $*OCCOH$ intermediates, respectively, which are key intermediates of C_{2+} products.[56,63,67] The $*OCCO$ intermediates appear at $\sim$1530 cm^{-1}, indicating that the C–C coupling mode on the catalyst is likely due to dimerization of the $*CO$ intermediate, leading to further

hydrogenation into $*OCCOH$.[68–70] As the applied voltage becomes more negative, the accumulation of $*CHO$ ($\sim$1041 and $\sim$1480 cm^{-1}) and the weakening of $*OCCHO$ ($\sim$1290 cm^{-1}) peak intensity on the Cu_2O-0 catalyst indicate that it is difficult to achieve C–C coupling of $*CO + *CHO$, which also indirectly confirms that the C–C coupling mode is $*CO + *CO$.[62,71]

The performance differences between Cu_2O-0 and Cu_2O-4 were understood by in-depth analysis of $*CO$ intermediates. Research findings suggest that the intermixing of $*CO_{bridge}$ and $*CO_{atop}$ was more favorable for the production of the C_{2+} products, which may be due to the ease of $*CO_{bridge}$ in promoting $*CO$ dimerization.[72] With the increase of negative voltage, the intensity of $*CO_{bridge}$ on Cu_2O-0 does not change obviously, but the intensity of the $*CO_{atop}$ first enhances and then decreases, indicating that $*CO$ intermediates accumulate first, and then more $*CO$ intermediates participate in the C–C coupling process on Cu_2O-0.[63] The change trend of $*CO_{atop}$ on the Cu_2O-0 catalyst in the *in situ* FT-IR spectrum is consistent with its *in situ* Raman spectrum (Fig. 4d). However, as the applied voltage increases, the $*CO_{bridge}$ peak ($\sim$1720 cm^{-1}) of the Cu_2O-4 catalyst decreases and almost disappears. At the same time, the intensity of the $*CO_{atop}$ peak ($\sim$2050 cm^{-1}) gradually increases (Fig. S33†), indicating that C–C coupling occurs with difficulty on the Cu_2O-4 catalyst.[63] The results of *in situ* FT-IR are consistent with those of *in situ* Raman and electrochemical CO_2RR.

DFT theoretical calculations

DFT theoretical calculations were used to gain a deeper understanding of the mechanism of Cu_2O-X catalysts promoting the electro-reduction of CO_2 to C_{2+} products. We
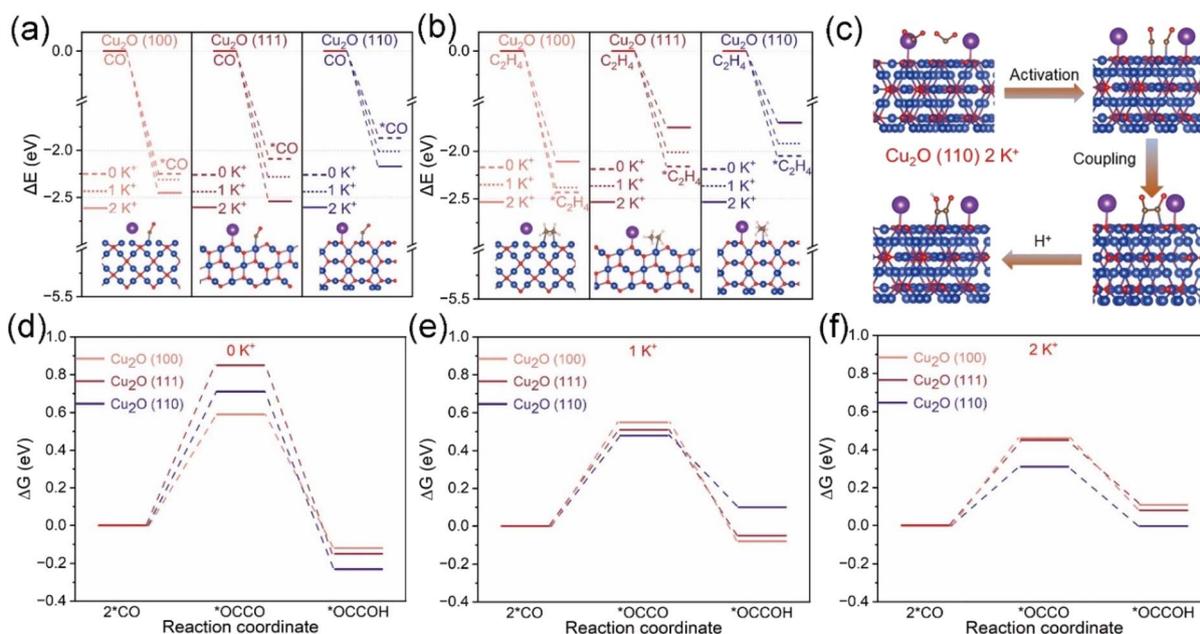
Fig. 5 Adsorption energies of (a) CO and (b) C_2H_4 on three crystalline surfaces of Cu_2O (100), (111) and (110) at three K^+ concentrations of 0 K^+, 1 K^+ and 2 K^+, respectively. (c) Adsorption configurations of reaction intermediates on the Cu_2O (110) structure at the K^+ concentrations of 2 K^+. Gibbs free energy pathways for C–C coupling on three crystalline surfaces of Cu_2O (100), (111) and (110) at three K^+ concentrations of 0 K^+ (d), 1 K^+ (e) and 2 K^+ (f), respectively.

performed DFT calculations to investigate the adsorption capacity of the reaction intermediate *CO and the product C_2H_4 at the Cu_2O (100), (111) and (110) interface at different K^+ concentrations as well as the Gibbs free energy of the C–C coupling. We developed a DFT model of the same Cu_2O crystal surface as the catalyst under study (Fig. S34†). As shown in Fig. 5a and b and S35–S40, and Tables S3 and S4,† *CO and *C_2H_4 adsorption on the Cu_2O (100) crystallite were stronger than that on Cu_2O (111) and (110) crystallites. It was very difficult for C_2H_4 to overflow from the Cu_2O (100) crystal surface, so the amount of C_{2+} product produced by the Cu_2O (100) crystal surface was low. Unlike the Cu_2O (100) crystal faces, the adsorption of *CO was weaker on the Cu_2O (111) and (110) crystal faces, but the introduction of K^+ led to the enhancement of *CO adsorption; at the same time, the adsorption of *C_2H_4 on the Cu_2O (111) and (110) crystal faces was weaker, and the C_2H_4 produced was readily desorbed out from the Cu_2O (111) and (110) crystal faces, so the amount of C_{2+} product produced by the Cu_2O (111) and (110) crystal faces was higher.

From the *in situ* characterization and DFT calculations (Fig. S41†), the pathway diagram of the Cu_2O-*X* catalyst to generate C_{2+} products was constructed and is shown in Fig. S42.†[61] The critical step to generate C_{2+} products is the coupling of two *CO intermediates into *OCCO intermediates. Fig. 5c shows the schematic diagram of the CO_2RR on the Cu_2O (110) crystal surface under 2 K^+ concentration. Fig. S43–S45† are schematic diagrams of the modeling of C–C coupling as well as hydrogenation. From Fig. 5d–f and S46–S49, and Table S5,† it is found that the Gibbs free energies of C–C coupling on all three crystalline surfaces of Cu_2O (100), (111) and (110) are decreasing with the increase of K^+ concentration. The Gibbs free energy of C–C coupling on the Cu_2O (110) (0.31 eV) and (111) (0.45 eV) crystal surfaces is smaller than that on the Cu_2O (100) (0.46 eV) crystal surface at 2 K^+ concentration, which suggests that the Cu_2O (110) and (111) crystal surfaces are more favorable for C–C coupling at high K^+ concentration. At the same time, experimental support was provided for the DFT calculation results (Fig. S50†). In the experiment, Cu_2O catalysts with different crystal planes were synthesized and the electrocatalytic CO_2 reduction performance was studied. It was found that the experimental results were consistent with the DFT calculation results.

Conclusions

In summary, we propose a strategy to enhance the field effect and thus improve the catalyst's performance for the electroreduction of CO_2 by changing the density of cubic corner arrays on the catalyst surface. CO_2RR experimental results indicated that the $FE_{C_{2+}}$ of the Cu_2O catalyst with high-density cubic corners was 71% at a partial current density of 497 mA cm^{-2}, and the $FE_{C_{2+}}$ of this Cu_2O-0 catalyst was 1.8 times higher than the $FE_{C_{2+}}$ of the microcubic Cu_2O catalyst. Moreover, the cubic corner arrays on the surface of Cu_2O microspheres help to improve the hydrophobicity of the catalyst and reduce the occurrence of its competing HER. FEM simulations and DFT calculations demonstrated that the high density of cubic corners contributed to the enhancement of the local electric field, which increased the K^+ concentration in the local microenvironment and enhanced the adsorption of *CO intermediates on the catalyst surface. The increase in the density of cubic corners leads to a higher number of vertices (Cu_2O (111)) and ridges (Cu_2O (110)). Relative to Cu_2O (100), Cu_2O (111) and Cu_2O (110) can effectively reduce the energy barrier of C–C coupling and improve the Faraday efficiency of C_{2+} products at high K^+ concentrations. This strategy can not only effectively improve the CO_2RR performance of the catalysts, but also indicates that the surface structure of the catalysts plays an important role in their CO_2RR performance, which provides a new idea for the design of efficient CO_2RR catalysts.

Data availability

Data supporting the findings of this study are available within the article ESI.†

Author contributions

Hu Zang: conceptualization, data curation, formal analysis, investigation, methodology, software, writing – original draft, and writing – review & editing; Changjiang Liu, Qinyuan Ji, Jiahao Wang, and Haiyan Lu: data curation, formal analysis, investigation, and software; Nan Yu: investigation, methodology, software and validation; Baoyou Geng: conceptualization, formal analysis, investigation, methodology, resources, funding acquisition, supervision, project administration, and writing – review & editing.

Conflicts of interest

The authors declare no conflicts of interest.

Acknowledgements

References

1 P. Falkowski, R. J. Scholes and E. Boyle, *Science*, 2000, **290**, 291–296.

2 B. Obama, *Science*, 2017, **355**, 126–129.

3 A. J. Welch, E. Dunn and J. S. Duchene, *ACS Energy Lett.*, 2020, **5**, 940–945.

4 X. Tan, C. Yu and Y. Ren, *Energy Environ. Sci.*, 2021, **14**, 765–780.

5 L. P. De, C. Hahn, D. Higgins, S. A. Jaffer, T. F. Jaramillo and E. H. Sargent, *Science*, 2019, **364**, eaav3506.

6 O. S. Bushuyev, L. P. De, C. T. Dinh, L. Tao, G. Saur, J. Lagemaat, S. O. Kelley and E. H. Sargent, *Joule*, 2018, **2**, 825–832.

7 T. M. Gür, *Energy Environ. Sci.*, 2018, **11**, 2696–2767.

8 D. F. Gao, R. M. Aran-ais and H. S. Jeon, *Nat. Catal.*, 2019, **2**, 198–210.

9 A. D. Handoko, F. X. Wei, Jenndy, S. Y. Boon and W. S. Zhi, *Nat. Catal.*, 2018, **1**, 922–934.

10 X. Mao, T. W. He, G. Kour, H. Q. Yin, C. Y. Ling, G. P. Gao, Y. G. Jin, Q. J. Liu, A. P. O'Mullane and A. J. Du, *Chem. Sci.*, 2024, **15**, 3330–3338.

11 H. R. M. Jhong, S. Ma and P. J. A. Kenis, *Curr. Opin. Chem. Eng.*, 2013, **2**, 191–199.

12 L. Zhu, Y. Lin, K. Liu, E. Cortes, H. Li, J. Hu, A. Yamaguchi, X. Liu, M. Miyauchi, J. Fu and M. Liu, *Chin. J. Catal.*, 2021, **42**, 1500–1508.

13 X. Zhi, Y. Jiao, Y. Zheng, K. Davey and S. Z. Qiao, *J. Mater. Chem. A*, 2021, **9**, 6345–6351.

14 T. Zhang, Z. Li, J. Zhang and J. Wu, *J. Catal.*, 2020, **387**, 163–169.

15 Y. C. Li, E. P. Delmo, G. Y. Hou, X. L. Cui, M. Zhao, Z. H. Tian, Y. Zhang and M. H. Shao, *Angew. Chem., Int. Ed.*, 2023, e202313522.

16 K. Yao, Y. Xia, J. Li, N. Wang, J. Han, C. Gao, M. Han, G. Shen, Y. Liu, A. Seifitokaldani, X. Sun and H. Liang, *J. Mater. Chem. A*, 2020, **8**, 11117–11123.

17 Y. D. Wang, R. Y. Zhao, Y. P. Liu, F. T. Zhang, Y. P. Wang, Z. H. Wu, B. X. Han and Z. M. Liu, *Chem. Sci.*, 2024, **15**, 4140–4145.

18 Z. Gu, H. Shen, Z. Chen, Y. Yang, C. Yang, Y. Ji, Y. Wang, C. Zhu, J. Liu, J. Li, T.-K. Sham, X. Xu and G. Zheng, *Joule*, 2021, **5**, 429–440.

19 H. Li, T. Liu, P. Wei, L. Lin, D. Gao, G. Wang and X. Bao, *Angew. Chem., Int. Ed.*, 2021, **60**, 14329–14333.

20 X. Zhang, K. Liu, J. Fu, H. Li, H. Pan, J. Hu and M. Liu, *Front. Phys.*, 2021, **16**, 63500.

21 B. Yang, K. Liu, H. Li, C. Liu, J. Fu, H. Li, J. E. Huang, P. Ou, T. Alkayyali and C. Cai, *J. Am. Chem. Soc.*, 2022, **144**, 3039–3049.

22 X. Zhang and Z. Zhou, *J. Phys. Chem. C*, 2022, **126**, 3820–3829.

23 S. Nitopi, E. Bertheussen, S. B. Scott, X. Liu, A. K. Engstfeld, S. Horch, B. Seger, I. E. L. Stephens, K. Chan, C. Hahn, J. K. Nørskov, T. F. Jaramillo and I. Chorkendorff, *Chem. Rev.*, 2019, **119**, 7610–7672.

24 G. Wang, J. Chen, Y. Ding, P. Cai, L. Yi, Y. Li, C. Tu, Y. Hou, Z. Wen and L. Dai, *Chem. Soc. Rev.*, 2021, **50**, 4993–5061.

25 M. B. Ross, P. De Luna, Y. Li, C. T. Dinh, D. Kim, P. Yang and E. H. Sargent, *Nat. Catal.*, 2019, **2**, 648–658.

26 X. Hu, S. Yao, L. T. Chen, X. Zhang, M. G. Jiao, Z. Y. Lu and Z. Zhou, *J. Mater. Chem. A*, 2021, **9**, 23515–23521.

27 P. S. Li, J. H. Bi, J. Y. Liu, Q. G. Zhu, C. J. Chen, X. F. Sun, J. L. Zhang, Z. M. Liu and B. X. Han, *Chem. Sci.*, 2023, **14**, 310–316.

28 K. Jiang, Y. Huang, G. Zeng, F. M. Toma, W. A. Goddard and A. T. Bell, *ACS Energy Lett.*, 2020, **5**, 1206–1214.

29 C. Tang, J. Shi, X. Bai, A. Hu, N. Xuan, Y. Yue, T. Ye, B. Liu, P. Li, P. Zhuang, J. Shen, Y. Liu and Z. Sun, *ACS Catal.*, 2020, **10**, 2026–2032.

30 Y. Wang, H. Shen, K. J. T. Livi, D. Raciti, H. Zong, J. Gregg, M. Onadeko, Y. Wan, A. Watson and C. Wang, *Nano Lett.*, 2019, **19**, 8461–8468.

31 Z. Sun, J. Dong, C. Chen, S. Zhang and Y. Zhu, *J. Chem. Technol. Biotechnol.*, 2021, **96**, 1161–1175.

32 Y. Zhou, F. Che, M. Liu, C. Zou, Z. Liang, P. De Luna, H. Yuan, J. Li, Z. Wang and H. Xie, *Nat. Chem.*, 2018, **10**, 974–980.

33 X. Tan, H. J. Zhu, C. He, Z. W. Zhuang, K. A. Sun, C. Zhang and C. Chen, *Chem. Sci.*, 2024, **15**, 4292–4312.

34 Y. Wang, P. Han, X. Lv, L. Zhang and G. Zheng, *Joule*, 2018, **2**, 2551–2582.

35 S. Y. Lee, S. Y. Chae, H. Jung, C. W. Lee, D. L. T. Nguyen, H. S. Oh, B. K. Min and Y. J. Hwang, *J. Mater. Chem. A*, 2020, **8**, 6210–6218.

36 L. P. De, B. R. Quintero, C. T. Dinh, M. B. Ross, O. S. Bushuyev, P. Todorovic, T. Regier, S. O. Kelley, P. Yang and E. H. Sargent, *Nat. Catal.*, 2018, **1**, 103–110.

37 Y. Y. Xue, Y. B. Guo, H. J. Cui and Z. Zhou, *Small Methods*, 2021, **5**, 2100736.

38 H. Zhang, C. H. He, S. M. Han, Z. Y. Du, L. Wang, Q. B. Yun, W. B. Cao, B. W. Zhang, Y.-H. Tian and Q. P. Lu, *Chin. Chem. Lett.*, 2022, **33**, 3641–3649.

39 Y. G. Gao, Q. Wu, X. Z. Liang, Z. Y. Wang, Z. K. Zheng, P. Wang, Y. Y. Liu, Y. Dai, M.-H. Whangbo and B. B. Huang, *Adv. Sci.*, 2020, **7**, 1902820.

40 M. Liu, Y. Pang, B. Zhang, P. De Luna, O. Voznyy, J. Xu, X. Zheng, C. T. Dinh, F. Fan, C. Cao, F. P. de Arquer, T. S. Safaei, A. Mepham, A. Klinkova, E. Kumacheva, T. Filleter, D. Sinton, S. O. Kelley and E. H. Sargent, *Nature*, 2016, **537**, 382–386.

41 Y. J. Zhou, Y. Q. Liang, J. W. Fu, K. Liu, Q. Chen, X. Q. Wang, H. M. Li, L. Zhu, J. H. Hu, H. Pan, M. Miyauchi, L. X. Jiang, E. Cortés and M. Liu, *Nano Lett.*, 2022, **22**, 1963–1970.

42 Z. Z. Niu, F. Y. Gao, X. L. Zhang, P. P. Yang, R. Liu, L. P. Chi, Z. Z. Wu, S. Qin, X. X. Yu and M. R. Gao, *J. Am. Chem. Soc.*, 2021, **143**, 8011–8021.

43 W. L. Zhu, Y. J. Zhang, H. Y. Zhang, H. F. Lv, Q. Li and S. H. Sun, *J. Am. Chem. Soc.*, 2014, **136**, 16132–16135.

44 W. L. Zhu, R. Michalsky, H. F. Lv, X. L. Sun, A. A. Peterson and S. H. Sun, *J. Am. Chem. Soc.*, 2013, **135**, 16833–16836.

45 S. Back, M. S. Yeom and Y. S. Jung, *ACS Catal.*, 2015, **5**, 5089–5096.

46 D. S. Chen, W. B. Yu, Z. Deng, J. Liu, J. Y. Jin, M. Wu, L. H. Chen and B. L. Su, *RSC Adv.*, 2015, **5**, 55520–55526.

47 T. T. Zhao, J. H. Li, J. D. Liu, F. M. Liu, K. Q. Xu, M. Yu, W. Xu and F. Y. Cheng, *ACS Catal.*, 2023, **13**, 4444–4453.

48 A. Xu, S. F. Hung, A. Cao, Z. Wang, N. Karmodak, J. E. Huang, Y. Yan, A. Sedighian Rasouli, A. Ozden, F. Y. Wu, Z. Y. Lin, H. J. Tsai, T. J. Lee, F. Li, M. Luo, Y. Wang, X. Wang, J. Abed, Z. Wang, D. H. Nam, Y. C. Li, A. H. Ip, D. Sinton, C. Dong and E. H. Sargent, *Nat. Catal.*, 2022, **5**, 1081–1088.

49 S. Jiang, K. Klingan, C. Pasquini and H. Dau, *J. Chem. Phys.*, 2019, **150**, 041718.

50 M. W. Fang, M. L. Wang, Z. W. Wang, Z. X. Zhang, H. C. Zhou, L. M. Dai, Y. Zhu and L. Jiang, *J. Am. Chem. Soc.*, 2023, **145**, 11323–11332.

51 X. Y. Chen, D. A. Henckel, U. O. Nwabara, Y. Y. Li, A. I. Frenkel, T. T. Fister, P. J. A. Kenis and A. A. Gewirth, *ACS Catal.*, 2020, **10**, 672–682.

52 W. Zhang, C. Huang, Q. Xiao, L. Yu, L. Shuai, P. An, J. Zhang, M. Qiu, Z. Ren and Y. Yu, *J. Am. Chem. Soc.*, 2020, **142**, 11417–11427.

53 G.-Y. Duan, X.-Q. Li, G.-R. Ding, L.-J. Han, B.-H. Xu and S.-J. Zhang, *Angew. Chem., Int. Ed.*, 2022, **61**, e202110657.

54 F. Li, Y. C. Li, Z. Wang, J. Li, D.-H. Nam, Y. Lum, M. Luo, X. Wang, A. Ozden, S.-F. Hung, B. Chen, Y. Wang, J. Wicks, Y. Xu, Y. Li, C. M. Gabardo, C.-T. Dinh, Y. Wang, T.-T. Zhuang, D. Sinton and E. H. Sargent, *Nat. Catal.*, 2020, **3**, 75–82.

55 A. Singhal, M. R. Pai, R. Rao, K. T. Pillai, I. Lieberwirth and A. K. Tyagi, *Eur. J. Inorg. Chem.*, 2013, **14**, 2640–2651.

56 M. Zheng, P. Wang, X. Zhi, K. Yang, Y. Jiao, J. Duan, Y. Zheng and S.-Z. Qiao, *J. Am. Chem. Soc.*, 2022, **144**, 14936–14944.

57 I. V. Chernyshova, P. Somasundaran and S. Ponnurangam, *Proc. Natl. Acad. Sci. U.S.A.*, 2018, **115**, E9261–E9270.

58 X. Wang, P. Ou, A. Ozden, S.-F. Hung, J. Tam, C. M. Gabardo, J. Y. Howe, J. Sisler, K. Bertens, F. P. G. de Arquer, R. K. Miao, C. P. O'Brien, Z. Wang, J. Abed, A. S. Rasouli, M. Sun, A. H. Ip, D. Sinton and E. H. Sargent, *Nat. Energy*, 2022, **7**, 170–176.

59 F. Li, A. Thevenon, A. Rosas-Hernández, Z. Wang, Y. Li, C. M. Gabardo, A. Ozden, C. T. Dinh, J. Li, Y. Wang, J. P. Edwards, Y. Xu, C. McCallum, L. Tao, Z.-Q. Liang, M. Luo, X. Wang, H. Li, C. P. O'Brien, C.-S. Tan, D.-H. Nam, R. Quintero-Bermudez, T.-T. Zhuang, Y. C. Li, Z. Han, R. D. Britt, D. Sinton, T. Agapie, J. C. Peters and E. H. Sargent, *Nature*, 2020, **577**, 509–513.

60 H. Y. An, L. F. Wu, L. D. B. Mandemaker, S. Yang, J. de Ruiter, J. H. J. Wijten, J. C. L. Janssens, T. Hartman and B. M. Weckhuysen, *Angew. Chem., Int. Ed.*, 2021, **60**, 16576–16584.

61 Y. W. Jiang, X. Y. Wang, D. L. Duan, C. H. He, J. Ma, W. Q. Zhang, H. J. Liu, R. Long, Z. B. Li, T. T. Kong, X. J. Loh, L. Song, E. Y. Ye and Y. J. Xiong, *Adv. Sci.*, 2022, **9**, 2105292.

62 F. Q. Yu, X. Liu, L. L. Liao, G. M. Xia and H. M. Wang, *Small*, 2023, 2301558.

63 C. Liu, M. M. Wang, J. Y. Ye, L. B. Liu, L. G. Li, Y. H. Li and X. Q. Huang, *Nano Lett.*, 2023, **23**, 1474–1480.

64 M. Liu, Q. Y. Wang, T. Luo, M. Herran, X. Y. Cao, W. R. Liao, L. Zhu, H. M. Li, A. Stefancu, Y.-R. Lu, T.-S. Chan, E. Pensa, C. Ma, S. G. Zhang, R. Y. Xiao and E. Cortés, *J. Am. Chem. Soc.*, 2024, **146**, 468–475.

65 S. Q. Zhu, T. H. Li, W.-B. Cai and M. H. Shao, *ACS Energy Lett.*, 2019, **4**, 682–689.

66 S. H. Min, X. Xu, J. X. He, M. Sun, W. L. Lin and L. T. Kang, *Small*, 2024, 2400592, DOI: 10.1002/smll.20240059.

67 Y. Zheng, A. Vasileff, X. Zhou, Y. Jiao, M. Jaroniec and S. Z. Qiao, *J. Am. Chem. Soc.*, 2019, **141**, 7646–7659.

68 Y. Kim, S. Park, S.-J. Shin, W. Choi, B. K. Min, H. Kim, W. Kim and Y. J. Hwang, *Energy Environ. Sci.*, 2020, **13**, 4301–4311.

69 H. Luo, B. Li, J. G. Ma and P. Cheng, *Angew. Chem., Int. Ed.*, 2022, **61**, e202116736.

70 J. Q. Feng, L. M. Wu, S. J. Liu, L. Xu, X. N. Song, L. B. Zhang, Q. G. Zhu, X. C. Kang, X. F. Sun and B. X. Han, *J. Am. Chem. Soc.*, 2023, **145**, 9857–9866.

71 W. C. Ma, S. J. Xie, T. T. Liu, Q. Y. Fan, J. Y. Ye, F. F. Sun, Z. Jiang, Q. H. Zhang, J. Cheng and Y. Wang, *Nat. Catal.*, 2020, **3**, 478–487.

72 Z. M. Wei, J. Ding, X. X. Duan, G.-L. Chen, F.-Y. Wu, L. Zhang, X. J. Yang, Q. Zhang, Q. Y. He, Z. Y. Chen, J. Huang, S.-F. Hung, X. Yang and Y. M. Zhai, *ACS Catal.*, 2023, **13**, 4711–4718.